10126 *Inorg. Chem.* **2009**, *48*, 10126–10137
DOI: 10.1021/ic901046f

Inorganic Chemistry
Article

Experimental and TDDFT Characterization of the Light-Induced Cluster-to-Iron Charge Transfer in the (Ferrocenylethynyl)-Substituted Trinuclear Platinum Derivative $[Pt_3(\mu\text{-}PBu^t_2)_3(CO)_2(C{\equiv}C{-}Fc)]^+$

Fabrizia Fabrizi de Biani,*,† Gabriele Manca,‡ Lorella Marchetti,‡ Piero Leoni,‡ Samantha Bruzzone,‡ Carla Guidotti,‡ Andrea Atrei,† Alberto Albinati,§ and Silvia Rizzato§

†*Dipartimento di Chimica dell'Università di Siena, Via A. De Gasperi 2, I-53100 Siena, Italy,* ‡*Dipartimento di Chimica e Chimica Industriale dell'Università di Pisa, Via Risorgimento, I-56126 Pisa, Italy, and* §*Dipartimento di Chimica Strutturale e Stereochimica Inorganica dell'Università di Milano, Via G. Venezian 21, I-20133 Milano, Italy*

Received May 31, 2009

The reaction between $Pt_3(\mu\text{-}PBu^t_2)_3(CO)_2Cl$ (**2**) and ethynylferrocene, in the presence of catalytic amounts of CuI, gives $Pt_3(\mu\text{-}PBu^t_2)_3(CO)_2C{\equiv}CFc$ (**1**), characterized by X-ray crystallography and representing a rare example of the σ-coordination of an alkynyl moiety to a cluster unit. In a dichloromethane (CH_2Cl_2) solution, compound **1** undergoes three consecutive one-electron oxidations, the first of which is assigned to the ferrocene-centered Fe^{II}/Fe^{III} redox couple. Spectroelectrochemistry, carried out on a solution of **1**, shows the presence of a broad band in the near-IR region, growing after the electrochemical oxidation, preliminarily associated with a metal-to-metal charge transfer toward the Fe^{III} ion of the ferrocenium unit. Density functional theory (DFT) has been employed to analyze the ground- and excited-state properties of **1** and $\mathbf{1}^+$, both in the gas phase and in a CH_2Cl_2 solution. Vertical excitation energies have been computed by the B3LYP hybrid functional in the framework of the time-dependent DFT approach, and the polarizable continuum model has been used to assess the solvent effect. Our results show that taking into account the medium effects together with the choice of an appropriate molecular model is crucial to correctly reproducing the excitation spectra of such compounds. Indeed, the nature of the substituents on P atoms has been revealed to have a key role in the quality of the calculated spectra.

Introduction

The basics of the design of a molecular device require the assembly of molecular fragments, affording an extended molecular system in which the "simple specific actions" of each component are cooperating to achieve a more complex function. Thus, the selected molecular components should be easily linked to each other, preferably in a predetermined shape, and the mechanism of their specific action as well as that of their possible mutual communication should be well understood.

We have recently reported that the tribridged trinuclear unit $[\{Pt_3\}L_{3-n}X_n]^{(1-n)+}$ ($\{Pt_3\} = [Pt_3(\mu\text{-}PBu^t_2)_3]^+$; $n = 0, 1$; L = neutral ligand; X = anionic ligand) and the tetrabridged hexanuclear unit $[\{Pt_6\}L_{6-n}X_n]^{(2-n)+}$ ($\{Pt_6\}=[Pt_6(\mu\text{-}PBu^t_2)_4]^{2+}$; $n = 0, 1, 2$) are very efficient synthons for the design of highly extended structures.[1,2] From a structural point of view, these clusters constitute interesting and versatile building blocks, in that they possess two or three reactive positions mutually directed at 180° or 120° for the hexa- and trinuclear units, respectively. In both cases, the electronic structure of the cluster units can be finely tuned, keeping the core unchanged, by choosing suitable terminal ligands.[1,2]

Moreover, because of a series of favorable properties (chemical robustness, synthetic versatility, and two stable redox states), ferrocenyl (Fc) or, more often, ferrocenylethynyl pendant groups have frequently been used to probe the electron-transfer ability of an attached redox-active unit.[3a] This strategy has been recently adopted in the case of $Pt_6(\mu\text{-}PBu^t_2)_4(CO)_4(C{\equiv}CFc)_2$, in which the $[\{Pt_6\}(CO)_4]^{2+}$ core is

*To whom correspondence should be addressed. E-mail: fabrizi@unisi.it.

(1) (a) Leoni, P.; Marchetti, L.; Mohapatra, S. K.; Ruggeri, G.; Ricci, L. *Organometallics* **2006**, *25*, 4226. (b) Albinati, A.; Leoni, P.; Marchetti, L.; Rizzato, S. *Angew. Chem., Int. Ed.* **2003**, *42*, 5990. (c) Leoni, P.; Marchetti, F.; Marchetti, L.; Pasquali, M. *Chem. Commun.* **2003**, 2372.

(2) (a) Bonaccorsi, C.; Fabrizi de Biani, F.; Funaioli, T.; Leoni, P.; Marchetti, F.; Marchetti, L.; Zanello, P. *Chem.—Eur. J.* **2008**, *14*, 847. (b) Cavazza, C.; Fabrizi de Biani, F.; Leoni, P.; Marchetti, F.; Marchetti, L.; Zanello, P. *Inorg. Chem.* **2009**, *48*, 1385. (c) Fabrizi de Biani, F.; Ienco, A.; Laschi, F.; Leoni, P.; Marchetti, F.; Marchetti, L.; Mealli, C.; Zanello, P. *J. Am. Chem. Soc.* **2005**, *127*, 3076. (d) Leoni, P.; Marchetti, F.; Pasquali, M.; Marchetti, L.; Albinati, A. *Organometallics* **2002**, *21*, 2176.

 Published on Web 10/02/2009

capped by two ferrocenylethynyl groups. Electrochemical and spectroelectrochemical studies have indicated that this compound is a rare example of a metallic cluster behaving as an electron donor versus a ferrocenium acceptor.[3b]

We report in this paper that the trinuclear cluster $\{Pt_3\}(CO)_2C{\equiv}CFc$ (**1**), upon ferrocenyl oxidation, similarly undergoes a photoinduced electron transfer from the cluster unit to the peripheral Fc subunit. The spectral features of the charge-transfer band are similar to those of $Pt_6(\mu\text{-}PBu^t_2)_4(CO)_4(C{\equiv}CFc)_2$; this fact was somehow unexpected, given that the $[\{Pt_3\}L_{3-n}X_n]^{(1-n)+}$ and $[\{Pt_6\}L_{6-n}X_n]^{(2-n)+}$ families display a very different redox pattern.[1,2] A related Pt → C≡CFc electron transfer at comparable wavelengths has also been reported some years ago by Sato et al. for the series of mononuclear platinum derivatives *trans*-$[(PPh_3)_2(Ar)PtC{\equiv}CFc]^+$.[4] It is therefore interesting to understand whether the electron transfer involves only the Pt center directly linked to the ethynylferrocenium group or the whole cluster. The present paper addresses this matter through a time-dependent density functional theory (TDDFT) study, giving evidence to the fact that the achievement of satisfactory theoretical results is strictly conditioned by the critical choice of a very realistic molecular model (together with the introduction of the solvent effect). The synthesis and structural characterization of **1** and the results of electrochemical and spectroelectrochemical studies are also reported.

Synthesis and Characterization

Cluster **1** was obtained by the CuI (1%)-catalyzed dehydrohalogenation reaction between equimolar amounts of $\{Pt_3\}(CO)_2Cl$[2b] and ethynylferrocene and was isolated in high (>90%) yield as an analytically pure red precipitate; X-ray-quality crystals were grown by the slow evaporation of a chloroform solution. Spectral parameters extracted from multinuclear NMR and IR spectra (see the Experimental Section) are in agreement with the corresponding parameters observed for many strictly related $\{Pt_3\}(CO)_2C{\equiv}CR$ (R = H, $SiMe_3$, CCH, $CCSiMe_3$, Ar) derivatives described previously.[2b]

The resonances observed in $^{31}P\{^1H\}$ and $^{195}Pt\{^1H\}$ NMR spectra are quite complex but were satisfactorily reproduced by computer simulation,[5] which gave the following set of parameters (numbering scheme as in Figure 1): [δ_{P1P3} = 167.4, δ_{P2} = 94.4, δ_{Pt2Pt3} = −5691.4, δ_{Pt1} = −6132.2, $^2J_{P1P2}$ = $^2J_{P3P2}$ = 129.3 Hz, $^2J_{P1P3}$ = 254 Hz, $^1J_{Pt2P2}$ = $^1J_{Pt3P2}$ = 1861 Hz, $^2J_{Pt1P2}$ = −98 Hz, $^1J_{Pt1P1}$ = $^1J_{Pt1P3}$ = 2132 Hz, $^1J_{Pt2P1}$ = $^1J_{Pt3P3}$ = 1877 Hz, $^2J_{Pt2P3}$ = $^2J_{Pt3P1}$ = −60 Hz, $^1J_{Pt2Pt1}$ = $^1J_{Pt3Pt1}$ = 936 Hz, $^1J_{Pt2Pt3}$ = 1736 Hz]. Detailed descriptions of the $^{31}P\{^1H\}$ and $^{195}Pt\{^1H\}$ NMR signals observed for analogous derivatives and figures showing experimental and simulated spectra may be found elsewhere[6] and will not be duplicated here.

X-ray Crystal Structure

There are two independent molecules in the asymmetric unit of compound **1**; an ORTEP view of the structure of one of the two "Pt_3 clusters" is shown in Figure 1, while the most relevant bond distances and angles are listed in Table 1.

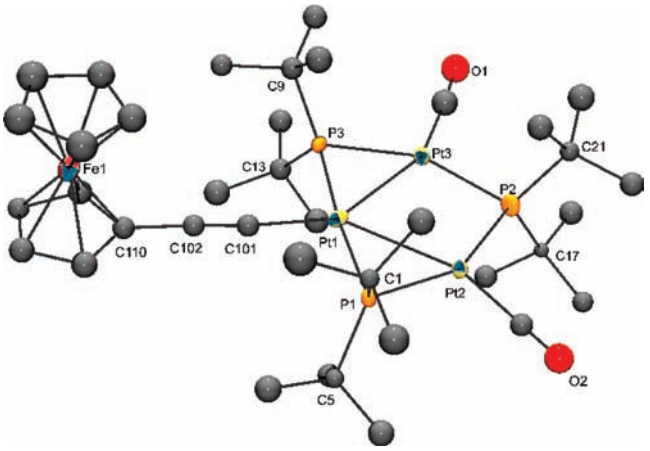

Figure 1. ORTEP view and numbering scheme for one of the two independent molecules in the asymmetric unit of **1** (Mol A). Thermal ellipsoids are drawn at 50% probability.

Table 1. Selected Bond Lengths (Å) and Angles (deg) in **1**[a]

	Mol A	Mol B
Pt1−Pt2	2.841(1)	2.870(1)
Pt1−Pt3	2.829(2)	2.860(2)
Pt2−Pt3	3.280(1)	3.208(1)
Pt1−P1	2.274(5)	2.272(5)
Pt1−P3	2.270(5)	2.278(5)
Pt2−P1	2.276(5)	2.290(5)
Pt2−P2	2.308(5)	2.310(6)
Pt3−P2	2.296(5)	2.319(4)
Pt3−P3	2.286(5)	2.296(5)
Pt1−C101	1.99(2)	1.97(2)
C101−C102	1.17(3)	1.20(3)
C102−C110	1.49(3)	1.44(3)
Fe−C (av)	2.05(3)	
Pt2−Pt1−Pt3	70.69(3)	68.12(3)
Pt1−Pt2−Pt3	54.48(3)	55.79(3)
Pt1−Pt3−Pt2	54.82(3)	56.09(3)
Pt1−P1−Pt2	76.6(2)	77.7(2)
Pt1−P3−Pt3	77.3(2)	78.0(2)
Pt2−P2−Pt3	90.9(2)	87.8(3)
Pt1−C101−C102	175(2)	178(2)
C101−C102−C110	177(2)	174(2)

[a] The numbering scheme corresponds to that used in Figure 1 (Mol A). The corresponding values for the second independent molecule are also listed (Mol B).

The overall geometries of the two molecules are very similar; however, few significant differences may be noticed.

In both molecules, the Pt atoms define approximately an isosceles triangle with two short and one long Pt−Pt separations (in the ranges 2.83−2.87 and 3.21−3.28 Å, respectively), with the largest separation being opposite to the ethynyl-substituted Pt center, a pattern that has also been observed in other $Pt_3(\mu\text{-}PR_2)_3L_2X$ complexes.[1,2] Moreover, the analogous Pt−Pt bond lengths in the two molecules are significantly different, as can be seen from the values listed in Table 1, while the Pt−P distances in the phosphido-bridging groups do not differ appreciably [av 2.279(7) Å for those bridging the shorter metal−metal bonds and 2.31(1) Å for the other two].

The Pt−Pt separations at 3.280(1) and 3.208(1) Å, although rather long, may still retain some bonding character and may

(3) (a) Barlow, S.; O'Hare, D. *Chem. Rev.* **1997**, *97*, 637. (b) Albinati, A.; Fabrizi de Biani, F.; Leoni, P.; Marchetti, L.; Pasquali, M.; Rizzato, S.; Zanello, P. *Angew. Chem., Int. Ed.* **2005**, *44*, 5701.

(4) Sato, M.; Mogi, E.; Katada, M. *Organometallics* **1996**, *14*, 4837.

(5) Budzelaar, P. H. M. *gNMR*, version 5.0.6.0; Adept Scientific plc: Herts, U.K., **2006**.

(6) Leoni, P.; Manetti, S.; Pasquali, M.; Albinati, A. *Inorg. Chem.* **1996**, *35*, 6045.

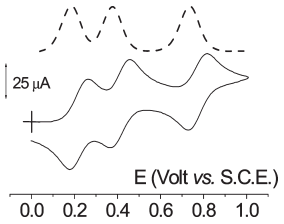

Figure 2. Cyclic (full) and Osteryoung square-wave (dotted) voltammograms recorded at a platinum electrode of a CH_2Cl_2 solution of **1**. $[NBu_4][PF_6]$ (0.2 mol dm^{-3}) supporting electrolyte. Scan rate: 0.2 V s^{-1}.

be compared with the average value of 3.618(2) Å found in $[Pt_3(\mu\text{-}PBu^t_2)_3(CO)_2H]$,[2c,6] the value of 3.171(1) Å found in $[Pt_3(\mu\text{-}PBu^t_2)_3(CNCH_3)_2H]$,[2d] and the sum of the Pt van der Waals radii, 3.4 Å. The wide range of distances spanned by the Pt−Pt separations in this class of triangular metal clusters is consistent with a remarkably soft potential for skeletal deformations and may be caused by nonbonding interactions.

The two molecules maintain the main features found in other $[\{Pt_3\}(L)_2X]$ moieties,[1,2]; i.e., the P atom, the ethynyl C atoms, and the C atom of the cyclopentadienyl ligand are lying on the least-squares plane defined by the three Pt atoms (maximum deviations for the P and ethynyl C atoms from this least-squares plane are approximately 0.1 Å, while for the C atoms of the Cp ring, they are 0.2 Å). As a consequence of coordination, the two cyclopentadienyl rings are not exactly staggered but are rotated by ca. 14° while remaining parallel, as can be judged from the values of the dihedral angle between the two rings: 3.2(8)° and 3.4(9)° for Mol A and Mol B, respectively. The remaining distances fall in the expected range.

The spatial distribution of the *tert*-butyl groups, symmetrically placed above and below the above-mentioned plane, is such as to offer steric protection to the inner Pt_3 core.

Electrochemistry and Spectroelectrochemistry

The previously reported electrochemical investigation[2b] on selected $[\{Pt_3\}(CO)_2X]$ (X = halide, alkynyl) or $[\{Pt_3\}L_3]^+$ (L = CO, isocyanide) derivatives was fundamental to gather information about their stability and its dependence on the nature of the ligand X. As a general feature, these clusters exhibit two one-electron oxidations, while, as expected, compound **1** undergoes a third one-electron Fc-centered oxidation (Figure 2). The pertinent redox potentials are reported in Table 2. By comparison with the general redox behavior of the related $[\{Pt_3\}(CO)_2X]$ series of clusters and of the strictly related $[\{Pt_3\}(CO)_2(C{\equiv}CPh)]$, also reported in Table 2, the second and third oxidations of **1** are assigned to the $\{Pt_3\}$ moiety, while the first one is assigned to ethynylferrocene. These assignments have been confirmed by spectroelectrochemistry and DFT calculations.

It is interesting to note that the ferrocene oxidation takes place at a potential of 340 mV less positive than that in free ethynylferrocene,[7] while the opposite shift is commonly observed in other metal−ethynylferrocenyl derivatives.[8] These data strongly suggest that the −C≡C− bridge allows a significant electronic interaction between the Fc and the cluster units, with the one-electron-oxidation product being stabilized by resonance over the two redox sites.

Table 2. Formal Electrode Potentials (V, vs SCE) and Peak-to-Peak Separations (mV) for the Redox Processes Exhibited by **1** and a Few Related Compounds (in a CH_2Cl_2 Solution)

	$\{Pt_3\}_{ox}$				Fc_{ox}	
compound	$E^{\circ\prime}$	ΔE_p[a]	$E^{\circ\prime}$	ΔE_p[a]	$E^{\circ\prime}$	ΔE_p[a]
$\{Pt_3\}(CO)_2(C{\equiv}CPh)$	+0.75[b]		+0.30	85		
$\{Pt_3\}(CO)_2(C{\equiv}CFc)$	+0.73	80	+0.37	85	+0.18	80
$HC{\equiv}CFc$[c]					+0.52	97

[a] Measured at 0.2 V s^{-1}. [b] Coupled to fast chemical reactions. [c] Data from ref 7.

A similar cathodic shift has been previously observed in the hexanuclear cluster $Pt_6(\mu\text{-}PBu^t_2)_4(CO)_4(C{\equiv}CFc)_2$[3b] (in which the oxidation of the ethynylferrocenyl ligand occurs at +0.30 V) as well as in the series of platinum derivatives *trans*-$[(PPh_3)_2(Ar)PtC{\equiv}CFc]$ (+0.26 to +0.23 V),[4] even if in such cases the effect was significantly smaller. Controlled potential coulometry of **1** (E_w = +0.25 V) in correspondence to the first anodic process confirms the consumption of one electron per molecule. The monocation $\mathbf{1}^+$ is relatively stable, as proven by the cyclic voltammograms recorded on the exhaustively oxidized solution, which appear essentially complementary to the original ones, except for the appearance of the weak signal at +0.61 V. On the other hand, cyclic voltammograms recorded after bulk electrolysis in correspondence to the second anodic process (E_w = +0.50 V) indicate that the dication $\mathbf{1}^{2+}$ tends to decompose slowly. In fact, the signal at +0.61 V becomes predominant.

The UV−vis spectral changes accompanying the first anodic process of **1** have been studied in situ in an optically transparent thin-layer (spectro)electrochemical (OTTLE) cell. As illustrated in Figure 3, the most significant spectral variation observed upon oxidation was the growing of a broad band in the near-IR (NIR) region (λ = 1135 nm; ε = 300 M^{-1} cm^{-1}), while the typical blue-to-green ferrocenium absorption (λ = 698 nm for $FcC{\equiv}CH^+$[7] was not detected. This feature is highly reminiscent of what has been observed upon stepwise two-electron oxidation of complex $[\{Pt_6\}(CO)_4(C{\equiv}CFc)_2]$[3b] and is similarly ascribed to a metal-to-metal charge transfer (MMCT) from the Pt_3 cluster to the ferrocenium subunit:

$$[\{Pt_3\}(CO_2)(C{\equiv}C\overset{\oplus}{Fc})] \xrightarrow{h\nu} [\{Pt_3^{\oplus}\}(CO_2)(C{\equiv}C\overset{\oplus}{Fc})]$$

The first oxidation of **1** has been also followed by IR spectroelectrochemistry in the OTTLE cell (Figure 4). Initially, the IR spectrum only exhibits the carbonyl stretching band at 2020 cm^{-1}; no C≡C stretching absorption was observed, suggesting a low polarity of the triple bond. Upon the first electron removal, the ν_{CO} absorption is blue-shifted by 6 cm^{-1}. The shift is too small to indirectly confirm that the first oxidation is actually centered on the Fc moiety. A new, weak, band at 2065 cm^{-1} also appears. This may confidently be ascribed to $\nu_{C\equiv C}$, the intensity of which is now enhanced by the polarization of the triple bond induced by the

(7) Fink, H.; Long, N. J.; Martin, A. J.; Opromolla, G.; White, A. J. P.; Williams, D. J.; Zanello, P. *Organometallics* **1997**, *16*, 2646.
(8) (a) Carugo, O.; Santis, G. D.; Fabbrizzi, L.; Licchelli, M.; Monichino, A.; Pallavicini, P. *Inorg. Chem.* **1992**, *31*, 765. (b) Rajput, J.; Moss, J. R.; Hutton, A. T.; Hendricks, D. T.; Arendse, G. E.; Imrie, C. *J. Organomet. Chem.* **2004**, *689*, 1553. (c) Barranco, E. M.; Cresspo, O.; Gimeno, M. C.; Jones, P. G.; Laguna, A.; Villacampa, M. D. *J. Organomet. Chem.* **1999**, *592*, 258.

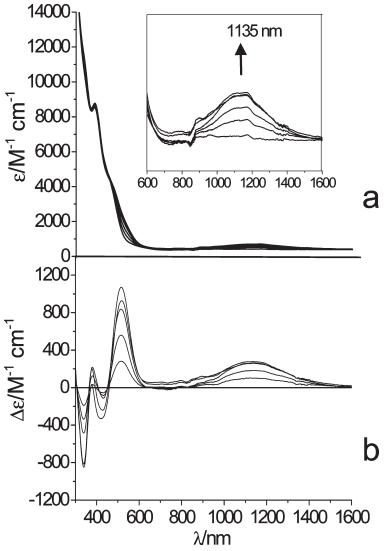

Figure 3. (a) UV−vis−NIR and (b) difference spectra recorded upon stepwise oxidation of **1** in a OTTLE cell in a CH_2Cl_2 solution ($[NBu_4][PF_6]$ = 0.2 mol dm^{-3}).

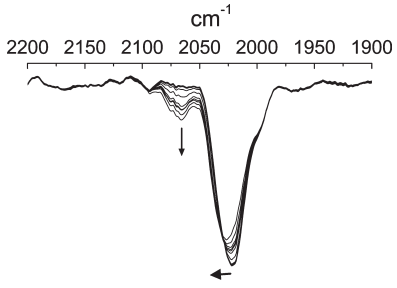

Figure 4. IR spectra recorded upon stepwise oxidation of **1** in a OTTLE cell in a CH_2Cl_2 solution ($[NBu_4][PF_6]$ = 0.2 mol dm^{-3}).

appended ferrocenium group. A nearly identical behavior has also been observed upon the stepwise oxidation of $\{Pt_6\}(CO)_4(C{\equiv}CFc)_2$.[9]

X-ray Photoelectron Spectroscopy (XPS) Results

XPS of complex **1** was carried out in order to obtain more direct evidence for the valency of the metal centers. In Figure 5, the Pt 4f XPS spectra measured for **1** and the halide derivative $[\{Pt_3\}(CO)_2Cl]$ (**2**) are shown together with those of the related platinum complexes $[Pt_2(\mu\text{-}P^tBu_2)_2(CO)_2]$ (**3**)[10] and $[Pt_2(\mu\text{-}P^tBu_2)_2(PH^tBu_2)_2H_2]$ (**4**)[11] (Chart 1), in which the formal Pt oxidation states are I and II, respectively. Pt $4f_{7/2}$ is located at a binding energy (BE) of 73.0 and 73.1 eV for **1** and **2**, respectively (Pt $4f_{7/2}$ and Pt $4f_{5/2}$ spin−orbit splittings = 3.3 eV).

The BE measured for **4** (Pt $4f_{7/2}$ = 72.4 eV) is lower than for **3** (Pt $4f_{7/2}$ = 72.8 eV). Although in contrast with what was expected considering platinum oxidation states, these results might be due to final states effects (i.e., the screening of the core hole in the Pt 4f levels) that can even reverse the order of

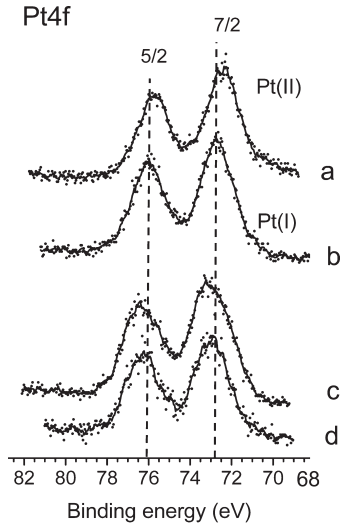

Figure 5. Pt 4f XPS spectra measured for (a) compound **4**, containing only Pt^{II}, (b) compound **3**, containing only Pt^{I}, (c) complex **2**, and (d) complex **1**. The Pt 4f peak appears as a doublet ($4f_{7/2}$ and $4f_{5/2}$) due to the spin−orbit splitting.

Chart 1

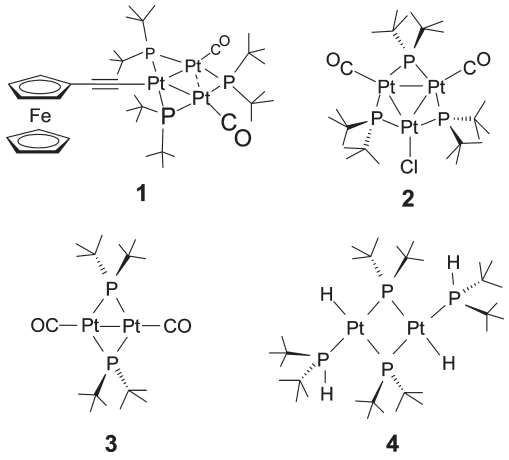

the BEs expected on the basis of the formal oxidation state. Anyway, the BEs measured for the nonequivalent Pt atoms are consistent with the actual electronic charge densities on the coordinated ions as derived by the DFT calculations (see below). This phenomenon actually mirrors the shortfall of the use of the oxidation state formalism as a confident estimate for the charge of an ion. As an obvious example, in compound **3**, the PtCO does not openly contribute to the oxidation state valuation of the Pt ions; nevertheless, it is well-known that π-back-donation reduces their electron content. As a matter of fact, according to the NIST X-ray Photoelectron Spectroscopy Database,[12] even the BEs measured for Pt^0 and Pt^{II} in the same cases overlap, ranging from 70.2 to 72 and from 71.8 to 75 eV, respectively. This confirms the dramatic effect of the nature and bonding mode of the ligands in determining the real charge of the coordinated ion.

Some interesting information can be deduced by comparing the two, more closely related, trinuclear complexes **1** and

(9) For $[\{Pt_6\}(CO)_4(C{\equiv}CFc)_2]$, ν_{CO} is at 2010 cm^{-1}; upon oxidation, the absorption is blue-shifted by 9 cm^{-1} and is accompanied by the appearance of a weak $\nu_{C\equiv C}$ band at 2074 cm^{-1}. Measurements were made in a $CH_2Cl_2/[NBu_4][PF_6]$ (0.2 mol dm^{-3}) solution.

(10) Albinati, A.; Leoni, P.; Marchetti, F.; Marchetti, L.; Pasquali, M.; Rizzato, S. *Eur. J. Inorg. Chem.* **2008**, *38*, 25.

(11) Leoni, P.; Manetti, S.; Pasquali, M. *Inorg. Chem.* **1995**, *34*, 749.

(12) Wagner, C. D.; Naumkin, A. V.; Kraut-Vass, A.; Allison, J. W.; Powell, C. J.; Rumble J. R. *NIST X-ray Photoelectron Spectroscopy Database*, version 3.4 (http://srdata.nist.gov/xps/index.htm).

2 and by the band-shape analysis of their spectrum. In these molecules, there are (at least formally) two Pt^{I} and one Pt^{II}. In fact, in particular for **2**, the Pt 4f peaks appear slightly asymmetric with a shoulder on the lower BE side, which suggests the existence of at least two components. The spectra were analyzed by a curve-fitting method including two components corresponding to the two nonequivalent types of Pt atoms in the molecules. The same full width at half-maximum (fwhm) and Gaussian−Lorentzian coefficient were used to fit all of the components. Because in each molecule two out of three Pt atoms are equivalent, we imposed the constraint that the area of one component is twice that of the other. The results of the curve-fitting analysis for **1** are shown in Figure S1 in the Supporting Information, and the main fitting parameters are reported in Table 3. For the Pt $4f_{7/2}$ peak, the components are located at 72.4 and 73.2 eV and at 72.1 and 73.2 eV for **1** and **2**, respectively. In both cases, the component at higher BE has twice the area of the other. It should be noted that the fitting of the Pt 4f peaks was significantly worse when forcing the component at lower BE to have twice the area of the component at higher BE.

According to this result, the BE of the two equivalent Pt atoms bonded to the carbonyl ligands is higher than the one measured for the Pt atom bonded to the chloride or ethynylferrocenyl ligands. This entails that the former are more positively charged than the latter, which again is in contrast with their formal oxidation states and, nonetheless, reasonable in light of the preceding discussion and in agreement with the DFT results discussed below.

We measured also the XPS spectra for the Fe 2p and P 2p regions; the Fe $2p_{3/2}$ peak appears at 708.3 eV, close to the values reported for ferrocene.[13] The P 2p peak is located at 130.6 eV. From the areas of the P 2p and Pt 4f peaks using literature atomic sensitivity factors,[14] the Pt/P atomic ratio turns out to be 1.1 ± 0.2, in agreement with the expected 1:1 atomic ratio.

Computational Studies

In order to address the question about the nature of the $\{Pt_3\}$/Fe charge transfer observed in the spectroelectrochemical study, we have performed a TDDFT analysis[15] on **1** and $\mathbf{1}^+$. It is known that the inclusion of the solvent environment in TDDFT calculations can give a more realistic description of charge-transfer processes;[16] for this reason, all of the calculations have been performed both in vacuo and in dichloromethane (CH_2Cl_2), by using the TDDFT method associated with the conductor-like polarizable continuum model (CPCM).[17]

Doing some preliminary calculations on simplified models in which the PBu^t_2 groups were replaced by PH_2 or PMe_2, we have observed that P substituents play a key role for the quality of the predicted electronic spectra. This specific effect was verified by running a series of calculations in which the nature of these substituents was varied, but otherwise the overall geometry of the systems was kept constant. We have decided to maintain the experimental structure of **1** also of **1**+ because the ferrocene/ferrocenium redox change is not expected to have a dramatic effect in the structure of the $\{Pt_3\}$ core and because the structure of the ferrocene itself is only slightly affected by the iron oxidation state.[18] Any successive attempt to optimize the geometry of $\mathbf{1}^+$ has failed to converge. The labeling of the atoms used in the following discussion is the same as that shown in Figure 1.

Table 3. Results of the Curve-Fitting Analyses for **1** and **2**[a]

	BE (eV)	
compound		
1	72.4 (1.85)	73.2 (1.85)
2	72.1 (1.68)	73.2 (1.68)

[a] Only the BEs of the two components of the Pt $4f_{7/2}$ peak (the fwhm's of the components are in parentheses) are reported. The BE scale was calibrated by setting the aliphatic component of the C 1s peak at 284.8 eV. The accuracy of the BE values is ±0.2 eV.

Electronic Structure. The electronic structure of **1** is nearly identical in vacuo and in CH_2Cl_2. Indeed, the solvent effect is to *rigidly* increase the energy of *all* molecular orbitals (MOs) by only 0.03 eV. A schematic representation of the energy levels for **1** calculated in CH_2Cl_2 is reported on the left side of Figure 6.

Earlier studies on the electronic structure of $[Pt_3(\mu\text{-}L')_3L_3]$ triangular metal clusters agree that, when the bridging ligands L′ are phosphido groups, there are two easily accessible frontier orbitals, very close in energy, the relative order of which may be easily reversed by several mechanisms, and that are in competition to be the highest occupied MO (HOMO). One of these is a radial metal−metal bonding combination (atomic orbitals point toward the center of the triangle), while the second one is better described as a tangential in-plane antibonding combination of Pt d orbitals (lying along the edges of the triangle) stabilized by interaction with the proper tangential antibonding combination of P p orbitals.[19]

According to our calculations, the HOMO of **1** actually corresponds to this latter description. The higher-lying group of filled orbitals is mainly Fe- or Pt_1-centered, or delocalized on both. More specifically, the four orbitals (HOMO−1)−(HOMO−4) arise from in-plane and out-of-plane bonding and antibonding combinations of Fe d and Pt d orbitals, mixed via the C≡C π system. The expected metal−metal radial bonding combination is found to be much lower in energy. Of the low-lying unoccupied orbitals (LUMOs), four arise from combinations of the CO π* systems, two (LUMO + 4 and LUMO + 6) are "pseudo-e_g" Fe d orbitals, and one (LUMO + 2)

(13) Woodbridge, C. M.; Pugmire, D. L.; Johnson, R. C.; Boag, N. M.; Langell, M. A. *J. Phys. Chem.* **2000**, *B104*, 3085.
(14) *Practical Surface Analysis*; Briggs, D., Seah, M.P., Eds.; Wiley: New York, 1985.
(15) (a) Stratmann, R. E.; Scuseria, G. E.; Frisch, M. J. *J. Chem. Phys.* **1998**, *109*, 8218. (b) Bauernschmitt, R.; Ahlrichs, R. *Chem. Phys. Lett.* **1996**, *256*, 454. (c) Casida, M. E.; Jamorski, C.; Casida, K. C.; Salahub, D. R. *J. Chem. Phys.* **1998**, *108*, 4439.
(16) (a) Vlček, A., Jr.; Záliš, S. *J. Phys. Chem. A* **2005**, *109*, 2991. (b) Villegas, J. M.; Stoyanov, S. R.; Reibenspies, J. H.; Rillema, D. P. *Organometallics* **2005**, *24*, 395. (c) Barone, V.; Fabrizi de Biani, F.; Ruiz, E.; Sieklucka, B. *J. Am. Chem. Soc.* **2001**, *123*, 10742.
(17) (a) Barone, V.; Cossi, M. *J. Phys. Chem.* **1998**, *A102*, 1995. (b) Cossi, M.; Rega, N.; Scalmani, G.; Barone, V. *J. Comput. Chem.* **2003**, *24*, 669.
(18) Zanello, P. *Inorganic Electrochemistry. Theory, Practice and Application*; Royal Society of Chemistry: Cambridge, U.K., 2003; and references cited therein.
(19) (a) Underwood, D. J.; Hoffmann, R.; Tatsumi, K.; Nakamura, A.; Yamamoto, Y. *J. Am. Chem. Soc.* **1985**, *107*, 5968. (b) Mealli, C. *J. Am. Chem. Soc.* **1985**, *107*, 2245. (c) Puddephatt, R. J.; Manojlovic-Muir, L.; Muir, K. W. *Polyhedron* **1990**, *9*, 2767. (d) Imhof, D.; Venanzi, L. M. *Chem. Soc. Rev.* **1994**, 185. (e) Burrows, A. D.; Mingos, D. M. P. *Coord. Chem. Rev.* **1996**, 154.

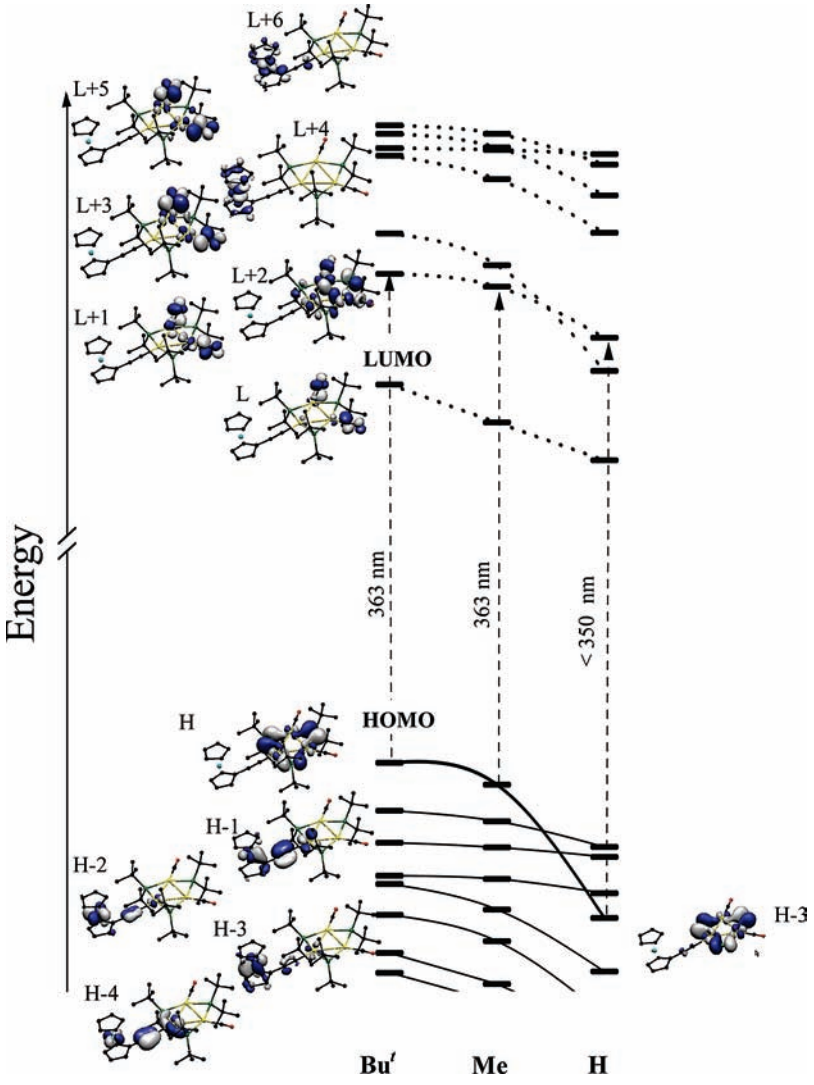

Figure 6. Frontier orbital energies for R = Bu^t, Me, and H in $Pt_3(\mu\text{-}PR_2)_3(CO)_2(C{\equiv}CFc)$, with calculations in CH_2Cl_2.

is mainly a σ-antibonding radial combination of CO with $Pt_{2,3}$ d orbitals. These features are caused by the inequality between Pt_1 and $Pt_{2,3}$, induced by the presence of the ethynylferrocene ligand, which affects also the Mulliken and natural bond orbital (NBO) population.[20] Actually, both methods suggest that Pt_1 is noticeably less positive than $Pt_{2,3}$ (Mulliken charges, Pt_1 = 0.03 vs $Pt_{2,3}$ = 0.22−0.32; NBO charges, Pt_1 = 0.08 vs $Pt_{2,3}$ = 0.17), consistent with what is observed in XPS spectra (see above).

Figure 7 shows the relative order of the α and β spin orbitals for the $S = {}^1/_2$ cation $\mathbf{1}^+$ in vacuo and in CH_2Cl_2. The cation has been treated by unrestricted calculations, so we will use the notation to call SO^{α} and SO^{β} the α and β spin orbital partners of a molecular orbital,[21] and therefore we will call HOSO and LUSO the highest occupied and lowest unoccupied molecular spin orbital, respectively. In this case, the effect of the solvent is outstanding. In CH_2Cl_2, the α and β spin orbitals are all destabilized; anyway different orbitals are destabilized to a different extent. Both in the presence of the solvent and in vacuo, the electronic relaxation due to electron removal modifies the shape of the orbitals with respect to those of complex **1**. In vacuo, a strong charge localization is unfavorable. In fact, even if the $LUSO^{\beta}$ is mostly Fe-centered, it is widely distributed also on the $\{Pt_3\}$ fragment. On the contrary, in the presence of the solvent, the charge can be much more localized, and the hole is left on the strongly Fe-centered $LUSO^{\beta}$. Indeed, the dipole moment calculated for $\mathbf{1}^+$, in both cases, points from the center of the Pt cluster toward the Fe ion, but its value changes greatly, being 7.9 and 22.9 D in vacuo and in the solvent, respectively.

The effect of a differently localized charge is mirrored by the rearrangement of the orbitals close to the frontier. First, because the charge is partially delocalized on both the $\{Pt_3\}$ cluster and the Fe center, in vacuo both $LUSO^{\beta}$ and $HOSO^{\beta}$ are lifted in energy with respect to the α counterpart, while in CH_2Cl_2, only $LUSO^{\beta}$ is lifted and $HOSO^{\beta}$ remains unaltered. Furthermore, in CH_2Cl_2, the Fe d orbitals are contracted and stabilized by the extra

(20) NBO version incorporated within the G03 suite: Glendening, E. D.; Carpenter, A. E.; Weinhold F. NBO Version 3.1; 1995.

(21) (a) Fox, M. A.; Roberts, R. L.; Khairul, W. M.; Hartl, F.; Low, P. J. *J. Organomet. Chem.* **2007**, *692*, 3277. (b) Powell, C. E.; Cifuentes, M. P.; McDonoagh, A. M.; Hurst, S. K.; Lucas, N. T.; Delfs, C. D.; Stranger, R.; Humphrey, M. G.; Houbrechts, S.; Asselberghs, I.; Persoons, A.; Hockless, D. C. R. *Inorg. Chim. Acta* **2003**, *9*, 352.

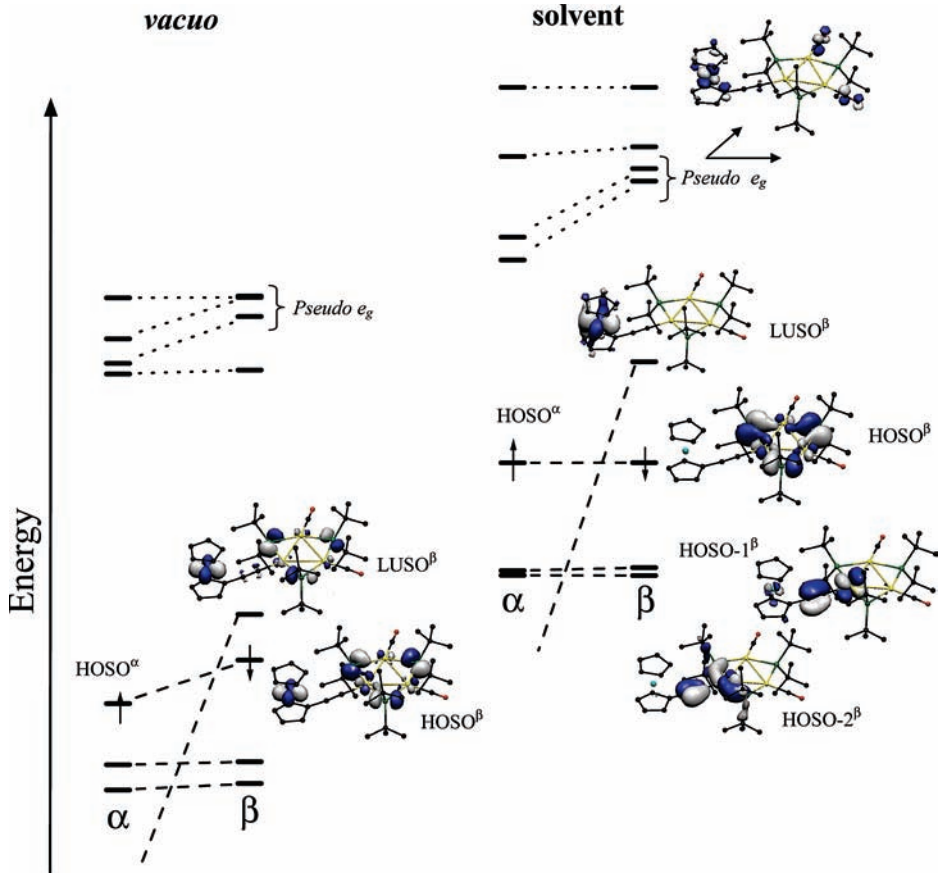

Figure 7. α and β spin orbitals for $\mathbf{1}^+$ in vacuo and in CH_2Cl_2.

positive charge, so that the "pseudo-e_g" couples are now the two lowest-lying empty orbitals. In vacuo, these orbitals are much less stabilized, and they are no longer the two lowest-lying empty orbitals.

Finally, in both cases, and at variance with what is observed for **1**, the three filled orbitals below HOSO are now much more localized on Pt_1. As we will discuss in the following paragraph, the different charge delocalizations, and its effects on the orbitals rearrangement, have a profound effect in the calculated electronic spectra.

Absorption Spectra. It has been shown that the virtual Kohn−Sham orbitals describe correctly the excited electrons and that the difference between the energies of virtual and occupied Kohn−Sham orbitals is a good approximation of the electronic transition energies.[22] Electronic transitions are represented by a linear combination of one-electron excitations between pairs of ground-state Kohn−Sham orbitals; therefore, the former procedure is appropriate only if the transitions are adequately described by a single one-electron excitation. In the next paragraph, we will show that the trend of the calculated wavelengths can be easily explained in terms of orbital energy differences, provided that a major single one-electron excitation contribution can be individuated.

The experimental spectra of **1** and $\mathbf{1}^+$ differ only in the lower energy region. Therefore, in all cases we calculated the first 30 excitation energies (15 lowest singlet−singlet and 15 lowest singlet−triplet excitation energies for **1**). These are enough to simulate the whole experimental

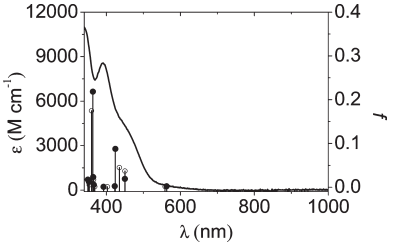

Figure 8. Comparison of the experimental spectrum of **1** and the calculated excitation energies and oscillator strengths calculated in CH_2Cl_2 (full circles) and in vacuo (open circles).

electronic spectrum of **1** as well as the low energy changes in the spectrum of $\mathbf{1}^+$.

A superposition of the experimental spectrum and the calculated excitation energies and oscillator strengths (f) of **1** in CH_2Cl_2 and in vacuo is reported in Figure 8. A detailed list of the wavelenghts calculated in vacuo and in the presence of the solvent is reported in Table 4, together with their relative oscillator strengths and the corresponding dominant MO transitions. The experimental spectrum shows four peaks at 535, 435, 391, and 340 nm. Actually, the best fit of the experimental spectrum is obtained with six closely spaced peaks at 541, 473, 424, 392, 360, and 340 nm (Table 4). We calculated nine absorptions with sizable oscillator strengths ($f \times 10^3 \geq 1$) in the same region.[23]

(22) Vlček, A., Jr.; Záliš, S. *Coord. Chem. Rev.* **2007**, *251*, 258.

(23) Many of the calculated values are very close in energy, and any attempt to reasonably fit the experimental spectrum by a Gaussian deconvolution with nine Gaussian curves yielded uncontrolled results due to overparametrization of the fitting procedure.

Table 4. Calculated TDDFT Singlet−Singlet Excitation Energies, Oscillator Strengths (in Parentheses), and Composition in Terms of the Main Orbital Transitions and Nature of the Electron Transfer for the Most Intense ($f \times 10^3 > 1$) Transitions for **1** in CH_2Cl_2 (Bold) and in Vacuo (Italics)[b]

λ/nm (f x10^3)	TDDFT main MO Transitions	nature of the transition	best fit peaks λ/nm (ε x10^{-3})	experimental peaks λ/nm (ε x10^{-3})
563 (2)	55% (HOMO-2) →(LUMO+4)	Fe d→ d	**541** (0.1)	**535** (0.5)
558 (2)	16% (HOMO-3) →(LUMO+6)			
	10% (HOMO-4) →(LUMO+4)			
450 (19)	28% (HOMO-8) →(LUMO+6)	Fe d→ d	**473** (0.6)	
450 (37)	24% (HOMO-3) →(LUMO+6)			
	12% (HOMO-1) →(LUMO+6)			
424 (88)	82% (HOMO-1) →(LUMO)	Pt_1, Fe→ CO π*		**435** (4.5)
435(45)			**424** (1.5)	
423 (3)	96% (HOMO) →(LUMO+1)	$\{Pt_3\}$ → CO π*		
-				
392 (1)	68% (HOMO-2) →(LUMO)	Pt_1, Fe→ CO π*	**392** (0.4)	
402(1)	26% (HOMO-4) →(LUMO)			
366 (6)	98% (HOMO-5) →(LUMO)	Pt_1 → CO π*		
368 (1)				
364 (22)	42% (HOMO-4) →(LUMO)	Pt_1, Fe→ CO π*		**391** (8.6)
365 (17)	14% (HOMO-2) →(LUMO)		**360** (6.3)	
	10% (HOMO-3) →(LUMO)			
363 (218)	70% (HOMO) →(LUMO+2)	$\{Pt_3\}$ → $\{Pt_3\}$		
359(174)				
353 (12)	32% (HOMO-3) →(LUMO)	Pt_1, Fe→ CO π*	**340** (0.8)	**340** (11.1)[a]
353(5)	18% (HOMO-8) →(LUMO+4)	Fe d→ d		
	12% (HOMO-2) →(LUMO+6)			

[a] Intensity stolen from the close UV absorption. [b] The best fit and experimental peaks with the associated molar extinction (in parentheses) are reported in the last two columns.

The inspection of Figure 8 and the comparison of the calculated wavelengths with the best fit or experimental ones confirm the nice agreement between experimental and theoretical data. A main concern regards the intense absorption at 391 nm, which is predicted to be very weak by the TDDFT calculations. We may, however, note that there are also two singlet−triplet excitations predicted at 398 and 383 nm that could contribute to the experimental spectrum but actually do not contribute to the calculated one because the TDDFT method used does not include spin−orbit coupling, and therefore their calculated f is null.

According to the TDDFT results, most of the nine electronic transitions calculated for **1** can be classified as metal-to-ligand charge transfer from Pt_1 and/or Fe to the CO π^* system. The weak absorption at 423 nm involves charge transfer from the $\{Pt_3\}$ core to the CO π^* system. The stronger absorption at 363 nm is a "core-to-core" ($\{Pt_3\}$ to $\{Pt_3\}$) transition, and the low-energy ones are Fe d → d transitions.

As could have been anticipated on the basis of its electronic structure, the calculated spectrum of cluster **1** is unaffected by the solvent, and, indeed, by fitting the wavelengths calculated in CH_2Cl_2 versus those obtained in vacuo, we obtained the linear relationship $h\nu^{Bu^t}{}_{solv}$ (eV) = $1.00h\nu^{Bu^t}{}_{vacuo}$ (eV) + 0.004 eV ($R = 0.995$; $P < 0.0001$).[24] Moreover, the substitution of the *tert*-butyl groups with methyl groups on the phosphido ligands causes an almost rigid red shift, and, in fact, a reliable linear relationship was found also in this case: $h\nu^{Bu^t}{}_{solv}$ (eV) = $0.91h\nu^{Me}{}_{solv}$ (eV) + 0.22 eV ($R = 0.982$; $P < 0.0001$), even if the oscillator strengths are not distinctly correlated.

Anyway, as soon as the *tert*-butyl groups are replaced by hydrogen atoms, a dramatic effect emerges; in fact, the intense experimental band found at 340 nm (correctly predicted at 363 nm with $f \times 10^3 = 2.2$ and $f \times 10^3 = 2.6$ with R = Bu^t or Me, respectively) suddenly "disappears" from the calculated spectrum. This can be explained by a close inspection of the orbitals close to the HOMO−LUMO frontier (Figure 7). In general, the energy of the orbitals decreases smoothly on passing from R = Bu^t to R = Me and R = H, but in some cases (when the orbitals have a relevant contribution by the phosphido groups), there is a sudden drop when R = H. This behavior reflects the increasing energy of the phospido orbitals when R becomes a stronger electron donor. The effects on the calculated spectrum are very significant. Concerning the absence of the band at 363 nm, what is observed (Table 4 and Figure 6) is that, for R = Bu^t, this absorption is mainly due to the HOMO−LUMO+2 transition. Both of these orbitals are stabilized when R = H, but the former goes much lower in energy. From Figure 6, we can see that the transition with the same nature is now the one from HOMO−3 to LUMO+1, reasonably expected to be blue-shifted far away from 363 nm and therefore not found in the calculated spectrum (calculated spectrum range up to 350 nm).

The nature of R is not only responsible for the altered orbital order but also for the different orbital mixing between Pt_1 and Fe, as is evident by checking the nature of

(24) P has its usual statistical meaning as "the probability of obtaining the correlation R when the data are uncorrelated".

Table 5. Calculated TDDFT Singlet−Singlet Excitation Energies, Oscillator Strengths (in Parentheses), and Composition in Terms of the Main Orbital Transitions and Nature of the Electron Transfer for the Most Intense ($f \times 10^3 > 1$) Transitions of $\mathbf{1}^{+b}$

λ/nm (f x10^3)	TDDFT main MO Transitions	nature of the transition	experimental peaks λ/nm (εx10^{-3})
1003 (7) *1783 (10)*	81% (HOSO-1)$^{\beta}$→ LUSO$^{\beta}$	Pt_1 → Fe	**1135** (0.3)
798 (4) *1281 (0)*	97% (HOSO-2)$^{\beta}$→ LUSO$^{\beta}$	Pt_1 → Fe	-
563 (6) *< 400*	84% (HOSO-1)$^{\alpha}$→ (LUSO)$^{\alpha}$	Pt_1 → Fe	**530** (a)
524 (46) *< 400*	74% (HOSO-1)$^{\alpha}$→ (LUSO+1)$^{\alpha}$	Pt_1 → Fe	

[a] Overlap with the peaks of the neutral compound. [b] Experimental peaks with the associated molar extinction (in parentheses) are reported in the last column.

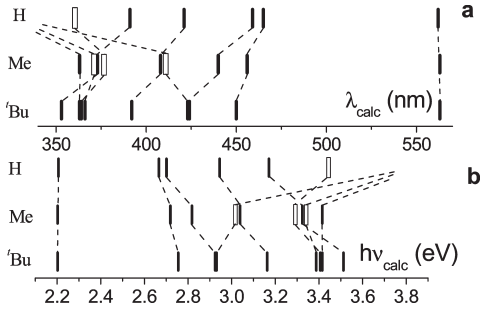

Figure 9. Changes in the excitation energies (a) λ_{calc} in nm and (b) $h\nu_{calc}$ in eV for R = Bu^t, Me, and H in $Pt_3(\mu\text{-}PR_2)_3(CO)_2(C{\equiv}CFc)$. Full lines: absorptions with $f \times 10^3 > 1$. Empty lines: absorptions with $f \times 10^3 < 1$.

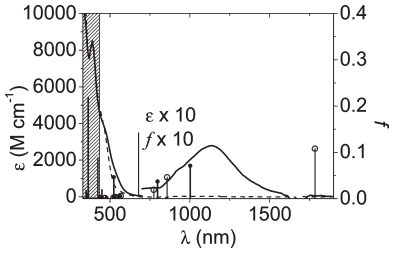

Figure 10. Comparison of the experimental spectrum of $\mathbf{1}^+$ and the calculated excitation energies and oscillator strengths calculated in CH_2Cl_2 (full circles) and in vacuo (open circles). The shadowed region has not been simulated by the TDDFT calculations. The spectrum of **1** is also shown (dotted line), together with the calculated excitation energies and oscillator strengths (in CH_2Cl_2, vertical bars).

the HOMO−1/HOMO−3 and HOMO−2/HOMO−4 pairs when R is Bu^t or H (Figure 6). These facts, together, not only modify the energy of the calculated wavelenghts but also alter the oscillator strengths. For these reasons, it is not straightforward to map out the transitions calculated for $[Pt_3(\mu\text{-}PH_2)_3(CO)_2(C{\equiv}CFc)]$ with those calculated for **1** or $[Pt_3(\mu\text{-}PMe_2)_3(CO)_2(C{\equiv}CFc)]$. Anyway, we could still sketch the related changes of the excitation energies by identifying each transition according to its nature in terms of the dominant single one-electron excitations. As graphically represented in Figure 9, by replacing Bu^t with H, some excitation energies are almost unchanged: these are Fe d → d transitions. In fact, in this case both the occupied and virtual orbitals, being mainly centered on Fe, undergo only minor variations. Another group of transitions are slightly red-shifted: these involve the transfer of one electron from the Pt_1−Fe-centered orbitals in which Pt_1 contributes with its out-of-plane d orbital to orbitals involving the π^* carbonyl system. In this case, the occupied orbitals do not mix with P (because Pt d is out-of-plane) and are insensitive to R, while all of the virtual orbitals slightly decrease in energy. Finally, some wavelengths are strongly blue-shifted and even disappear from the range of the calculated spectrum: in this case, the dominant excitations involve the transfer of one electron from occupied orbitals with an important P contribution (which steeply decrease when R = H) to whichever virtual orbital.

As an example, the couple of transitions at 424 nm (HOMO−1 → LUMO) and 423 nm (HOMO → LUMO + 1), calculated at very close values for **1**, are splitted to 440 nm (red shift, HOMO−1 → LUMO) and 411 nm (blue shift, HOMO → LUMO + 1) for $[Pt_3(\mu\text{-}PMe_2)_3(CO)_2(C{\equiv}CFc)]$ and to 459 nm (red shift, HOMO → LUMO) and > 350 nm (blue shift, HOMO−3 → LUMO + 2) for $[Pt_3(\mu\text{-}PH_2)_3(CO)_2(C{\equiv}CFc)]$, respectively.

The experimental absorptions, calculated excitation energies, and oscillator strengths of $\mathbf{1}^+$ in CH_2Cl_2 and in vacuo are compared in Figure 10. A detailed list of the excitation energies is reported in Table 5 together with the relative oscillator strengths and the corresponding dominant MO transitions. Two main features distinguish the experimental spectrum of $\mathbf{1}^+$ from that of **1**: the evident appearance of a shoulder at ∼530 nm and the growth of a weak and broad band in the NIR region at 1135 nm. The TDDFT results obtained by calculations in vacuo do not fit at all of the experimental spectrum, especially in the lower energy region (first four absorptions calculated at 1783, 858, 774, and 568 nm; NIR band not reproduced). In fact, as explained above, the calculated spectrum is severely altered in vacuo. Instead, the main features of the experimental spectrum are reproduced reasonably well by including solvent effects (the two excitations corresponding to the NIR and the shoulder bands are calculated at 1003 and 563−524 nm, respectively), even if the energy of the NIR absorption is slightly overestimated.

The NIR band is due to a Pt_1-to-ferrocenium charge-transfer process such as those observed in the series of mononuclear platinum derivatives *trans*-$[(PPh_3)_2(Ar)PtC{\equiv}CFc]^+$ described by Sato et al.[4] In this respect, it is interesting to notice that the NIR band involves the electron transfer from the Pt center directly linked to the

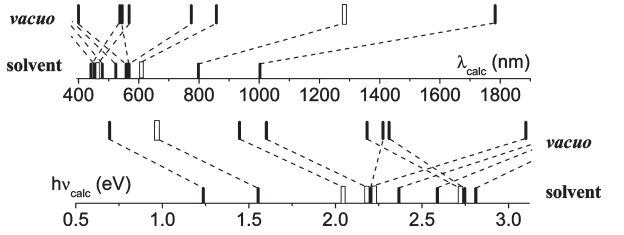

Figure 11. Changes in the calculated excitation energies for **1** in CH_2Cl_2 and in vacuo: (a) λ_{calc} in nm and (b) λ_{calc} in eV. Full lines: absorptions with $f > 1 \times 10^3$. Empty lines: absorptions with $f < 1 \times 10^3$.

ethynylferrocenium group rather than the whole $\{Pt_3\}$ cluster and, on the basis of the match of the NIR spectra, a similar event is expected also for the hexanuclear Pt cluster $[Pt_6(\mu\text{-}PBu^t_2)_4(CO)_4(C{\equiv}CFc)_2]^{+}$ [3b] On the other hand, because the Pt orbitals involved in the charge transfer are not the redox orbitals, these clusters may have a different redox pattern, as observed.

Actually, *all* of the four calculated excitations compiled in Table 5 arise from in-plane and out-of-plane Pt_1 d orbitals to ferrocenium charge transfers: two low-energy bands to the Fe-centered $LUSO^{\beta}$ and two higher-energy bands to the Fe "pseudo-e_g"$^{\alpha}$ orbitals.

There is also a weak absorption calculated at 798 nm and not observed in the experimental spectrum. Reasonably, the energy of this excitation may also be overestimated to some extent, so that in the experimental spectrum it is possibly hidden in the broad NIR band.

Once again, to explain the effect of the solvent, we may map the transitions calculated in vacuo to those calculated in the solvent according to their nature in terms of the dominant single one-electron excitations. The oscillator strengths may be different in the two cases because of some changes of the orbital shape. The results are graphically represented in Figure 11.

The solvent effect rigidly *blue-shifts* a group of transitions by ~0.57 eV ($h\nu^{Bu^t+}{}_{solv}$ (eV) = 0.99$h\nu^{Bu^t+}{}_{vacuo}$ (eV) + 0.57 eV; $R = 0.998$; $P < 0.0001$). However, in the presence of the solvent, a couple of transitions appear (at 563 and 524 nm) that had not been found in the spectrum calculated in vacuo (up to 400 nm). These are plausibly *red-shifted* by the solvent. A look at Figure 7 allows one to easily understand this behavior. In the blue-shifted group, the dominant MO transitions involve a transfer to $LUSO^{\beta}$. This is lifted in energy much more in the solvent than in vacuo, so that any transition from the occupied β orbitals to $LUSO^{\beta}$ would require more energy in the solvent than in vacuo.

On the contrary, in the red-shifted group, the dominant MO transitions involve charge transfer to the Fe "pseudo-e_g"$^{\alpha}$ orbitals. In the presence of the solvent, these are contracted and stabilized by the *extra* positive charge, so that any transition from occupied α orbitals to "pseudo-e_g"$^{\alpha}$ ones would require less energy in the solvent than in vacuo.

We will finally discuss the joint effect of the different substituents on the phosphido bridges by looking at the changes of the values calculated for the NIR band (Table 6). A relationship between $h\nu_{calc}$ and $\Delta\varepsilon_{LUSO^{\beta}/(HOSO-1)^{\beta}}$ (calculated for R = H, Me, or Bu^t in CH_2Cl_2 and in vacuo) is confirmed by the subsistence of the linear trend $h\nu_{calc}$ (eV) = 0.83 and $\Delta\varepsilon_{LUSO^{\beta}/(HOSO\text{-}1)^{\beta}}$ (eV) + 0.5 eV ($R = 0.996$; $P < 0.0001$) obtained by using all six NIR excitation energies.

Table 6. Calculated TDDFT Excitation Energies and Oscillator Strengths (in Parentheses) for the NIR Transition of $[Pt_3(\mu\text{-}PR_2)_3(CO)_2(C{\equiv}CFc)]^{+}$ in CH_2Cl_2 and in Vacuo

	λ, nm ($f \times 10^3$)	
R	in vacuo	in CH_2Cl_2
H	1146 (8)	834 (5)
Me	1410 (13)	948 (6)
Bu^t	1783 (11)	1003 (7)

Both in vacuo and in solution, this absorption is red-shifted on passing from R = Bu^t to R = Me and H. This can be explained by looking at the trend of the β frontier orbitals (Figure S2 in the Supporting Information). In fact, in any medium, the energy of $LUSO^{\beta}$, which is mostly Fe-centered, is almost unaffected by the nature of R, while the energy of Pt-centered $(HOSO\text{-}1)^{\beta}$ decreases slightly in the same series. Finally, it should be noticed that, whatever the nature of R, the solvent causes a blue shift of the NIR band. Such a behavior has been explained in detail for the case R = Bu^t.

At first sight, it seems rather puzzling that the solvent effect on the energy shift is more important for the bulky Bu^t substituents (0.54 eV) than for the smaller Me and H groups (0.43 and 0.40 eV, respectively) because the more sizable Bu^t groups should shield the compound and therefore reduce the solvent effect. However, we must consider that only the Pt_3 region of the system is protected by the Bu^t groups, while the ferrocenium is equally exposed to the solvent whatever the nature of R. As a result, in all cases, $LUSO^{\beta}$, mostly Fe-centered, is similarly destabilized by the presence of the solvent, while $(HOSO\text{-}1)^{\beta}$, mostly Pt_1-centered, is less destabilized in the case of R = Bu^t because these groups are an efficient screen for the Pt ion. The consequence is the enhanced blue shift observed for this latter case. We can look at this effect from another point of view: as stated before in vacuo, a strong charge localization is unfavorable; anyway, it is apparent, by looking at Figure S2 in the Supporting Information, that the (de)localization of the positive charge is affected by R, while this effect vanishes in the presence of the solvent because, in this latter case, the positive charge is always mostly localized on Fe. As a consequence, for R = Bu^t, there is an *extra* destabilization of $LUSO^{\beta}$ in the solvent, due to charge localization. As a matter of fact, it is possible to obtain a linear fit between the energy shift of the NIR band and the difference of the dipole moment in the solvent and in vacuo: $\Delta h\nu_{calc}$ (eV) = 0.01$\Delta\mu_{solv\text{-}vac}$ + 0.36 eV ($R = 0.996$; $P = 0.05$), shown in Figure S3 in the Supporting Information.

Conclusions

The trinuclear Pt cluster **1** exhibits a rich redox chemistry and an interesting spectroelectrochemical behavior, displaying an MMCT upon oxidation. In this work, we have enlightened many interesting features of this compound: XPS and DFT have revealed a counterintuitive charge distribution on the Pt ions, while TDDFT calculations have elucidated the nature of the bands in the electronic spectrum of the neutral and cationic compounds **1** and $\mathbf{1}^{+}$ and, at the same time, have outlined the importance of the peripheral substituents and the hazard to use oversimplified models. In

fact, while the importance of taking into account the presence of the solvent when trying to theoretically reproduce the charge-transfer features of an electronic spectrum is well-known and widely accepted, the use of simplified models is still very common. To the best of our knowledge, this is the first time that the influence of the nature of peripheral groups has been investigated in systems of similar complexity. The rich redox behavior of complex **1** and its charge-transfer attitude provide further evidence of the fact that these clusters may be employed as synthons in the design and synthesis of extended structures, whose shape and properties may be programmed in advance.

Experimental Section

1. Synthesis. The reactions were carried out under a nitrogen atmosphere, by using standard Schlenk techniques. $Pt_3(\mu\text{-}PBu_2^t)_3(CO)_2Cl$ was prepared as described previously.[2b] Solvents were dried by conventional methods and distilled under nitrogen prior to use. IR spectra (Nujol mulls, KBr) were recorded on a Perkin-Elmer FT-IR 1725X spectrophotometer. NMR spectra were recorded on a Varian Gemini 200 BB instrument (200 MHz for ^{1}H, 81.0 MHz for ^{31}P, 42.8 MHz for ^{195}Pt); chemical shifts are referenced to the residual resonances of the deuterated solvent (H, ^{13}C), 85% H_3PO_4 (^{31}P), and H_2PtCl_6 (^{195}Pt).

Preparation of $Pt_3(\mu\text{-}PBu_2^t)_3(CO)_2C{\equiv}CFc$. Ethynylferrocene (28.35 mg, 0.135 mmol) and CuI (0.257 mg, 1.35 μmol) were added to a red diethylamine solution of $Pt_3(\mu\text{-}PBu_2^t)_3(CO)_2Cl$ (150 mg, 0.135 mmol). After 24 h of stirring, the solvent was removed in vacuo. The red residue was extracted with diethyl ether. After chromatography on silica gel, using 1:2 CH_2Cl_2/hexane as the eluent, 155 mg of $Pt_3(\mu\text{-}PBu_2^t)_3(CO)_2C{\equiv}CFc$ was obtained (90.5% yield). Anal. Calcd for $C_{38}H_{63}FeO_2P_3Pt_3$: C, 35.5; H, 4.94. Found: C, 35.3; H, 4.86. ^{1}H NMR: δ 1.35 (d, ^3J(H,P) = 15.2 Hz, 18 H, CH_3), 1.47 (vt, ^3J(H,P) + ^5J(H,P) = 7.2 Hz, 36 H, CH_3), 4.12 (t, ^3J(H,H) = 1.8 Hz, 2 H, Cp, α C≡C), 4.17 (s, 5 H, Cp), 4.38 ppm (t, ^3J(H,H) = 1.8 Hz, 2 H, Cp, β C≡C). ^{13}C{^{1}H} NMR: δ 175 (s, ^1J(C,Pt) = 2019 Hz, ^2J(C,Pt) = 125, 44 Hz, CO), 118.0 (s, ^2J(C,Pt) = 470 Hz, Pt−C≡*C*), 79.0 (s, ^1J(C,Pt) = 1646 Hz, Pt−*C*≡C), 70.4 (s, C_5H_4), 69.5 (s, Cp), 67.0 (s, C_5H_4), 38.9, 38.6 (s, CCH_3), 33.5, 33.3 ppm (s, CH_3). IR (CH_2Cl_2): 2103 (C≡C), 2018 (CO) cm^{-1}.

2. Crystallography. Air-stable, red crystals of **1** were obtained, only of poor quality, by crystallization from chloroform. A crystal of **1** was mounted on a Bruker APEX diffractometer, for cell constant determination and data collection. The cell constants and diffraction symmetry unambiguously established the triclinic symmetry, while the centrosymmetric choice for the space group ($P\bar{1}$) was later confirmed by the successful refinement. The cell constants were refined, at the end of the data collection, with the data reduction software *SAINT*.[25] The experimental conditions for the data collection and crystallographic and other relevant data are listed in Table 7 and in the Supporting Information. The collected intensities were corrected for Lorentz and polarization factors.[25] The absorption correction proved to be difficult because of the very large absorption and the very irregular shape of the crystal. Two empirical absorption procedures were tried using the *SADABS* and *XABS* programs.[26,27] The latter gave a more satisfactory result as judged by the lower *R* factors and more realistic anisotropic displacement parameters for the heavy atoms. The structure was solved by direct and Fourier methods and refined by full-matrix least squares,[28] minimizing the function $[\sum w(F_o^2 - (1/k)F_c^2)^2]$ and using anisotropic displacement parameters for the Pt, P, and Fe atoms and isotropic parameters for the others. The contribution of the H atoms, in their calculated positions, was included in the refinement using a riding model with B(H) = aB(C-bonded) (Å^2) (where a = 1.5 for the H atoms of the methyl groups and a = 1.3 for the others). No extinction correction was deemed necessary. Upon convergence, the final Fourier difference map showed no significant peaks. The scattering factors used, corrected for the real and imaginary parts of the anomalous dispersion, were taken from the literature.[29] All calculations were carried out by using the PC version of the programs *WINGX*,[30] *SHELX-97*,[28] and *ORTEP*.[31]

Table 7. Experimental Data for the X-ray Diffraction Study of Compound **1**

formula	$C_{38}H_{63}FeO_2P_3Pt_3$
mol wt	1285.91
data collection T, K	293(2)
cryst syst	triclinic
space group	$P\bar{1}$ (No. 2)
a, Å	11.980(4)
b, Å	15.807(5)
c, Å	24.040(8)
α, deg	73.148(7)
β, deg	88.767(8)
δ, deg	88.162(7)
V, Å^3	4354(2)
Z	4
ρ_{calcd}, g cm^{-3}	1.962
μ, mm^{-1}	10.074
radiation	Mo Kα (graphite monochromatized, λ = 0.710 73 Å)
θ range, deg	0.89 < θ < 26.10
no. of indep data points	17 067
no. of obsd reflns (n_o) [$\lvert F_o\rvert^2 > 2.0\sigma(\lvert F\rvert^2)$]	9720
no. of param refined (n_v)	447
R (obsd reflns)[a]	0.0794
R_w^2 (obsd reflns) [b]	0.1776
GOF[c]	0.935

[a] $R = \sum(\lvert F_o - (1/k)F_c\rvert)/\sum\lvert F_o\rvert$. [b] $R_w^2 = \{\sum[w(F_o^2 - (1/k)F_c^2)^2]/\sum w\lvert F_o^2\rvert^2]\}^{1/2}$. [c] GOF = $[\sum_w(F_o^2 - (1/k)F_c^2)^2/(n_o - n_v)]^{1/2}$.

3. Electrochemistry and Spectroelectrochemistry. Anhydrous 99.9%, HPLC-grade CH_2Cl_2 for electrochemistry was purchased from Aldrich. The supporting electrolyte used was electrochemical-grade NBu_4PF_6 obtained from Fluka. Cyclic voltammetry was performed in a three-electrode cell having a platinum working electrode surrounded by a platinum-spiral counter electrode and an aqueous saturated calomel reference electrode (SCE) mounted with a Luggin capillary. Either a BAS 100A or a BAS 100W electrochemical analyzer was used as the polarizing unit. Hydrodynamic voltammetry made use of a platinum electrode with periodic renewal of the diffusion layer, obtained by moving the solid electrode with a time-controlled knocker. Controlled potential coulometry was performed in an H-shaped cell with anodic and cathodic compartments separated by a sintered-glass disk. The working macroelectrode was a platinum gauze; a mercury pool was used as the counter electrode. All reported potential values are referred to the SCE. Under experimental conditions, one-electron oxidation of ferrocene occurs at $E^{\circ\prime}$ = +0.39 V.

UV−vis spectroelectrochemical measurements were carried out using a Perkin-Elmer Lambda 900 UV−vis spectrophotometer and an OTTLE cell equipped with a platinum-minigrid working electrode (32 wires cm^{-1}), a platinum minigrid

(25) *BrukerAXS, SAINT*, Integration Software; Bruker Analytical X-ray Systems: Madison, WI, **1995**.
(26) Sheldrick, G. M. *SADABS, Program for Absorption Correction*; University of Göttingen: Göttingen, Germany, **1996**.
(27) Parkin, S.; Moezzi, B.; Hope, H. *J. Appl. Crystallogr.* **1995**, *28*, 53.
(28) Sheldrick, G. M. *Acta Crystallogr.* **2008**, *A64*, 112.
(29) *International Tables for X-ray Crystallography*; Wilson, A. J. C., Ed.; Kluwer Academic Publisher: Dordrecht, The Netherlands, 1992; Vol. *C*.
(30) Farrugia, L. J. *J. Appl. Crystallogr.* **1999**, *32*, 837–838.
(31) Farrugia, L. J. *J. Appl. Crystallogr.* **1997**, *30*, 565.

auxiliary electrode, a silver wire pseudoreference, and CaF_2 windows.[32] During the microelectrolysis procedures, the electrode potential was controlled by an Amel potentiostat 2059 equipped with an Amel function generator 568. Nitrogen-saturated CH_2Cl_2 solutions of the compound under study were used with $[NBu_4][PF_6]$ (2.0×10^{-3} mol dm^{-3}) as the supporting electrolyte. The in situ spectroelectrochemistry was recorded by collecting spectra in the spectral window of 220−3300 nm during the stepwise oxidation of the compound (Δt = 2 min; E_w = +0.25 V).

4. XPS. The XPS spectra were recorded using an apparatus (VSW limited) equipped with a hemispherical electron energy analyzer. Non-monochromatized Mg Kα radiation (1253.6 eV) was utilized as an excitation source with a power of 180 W. The spectra were collected with a constant pass energy of 22 eV. We did not observe any variation in the shape or position of the Pt 4f peaks upon an increase in the acquisition time, which could indicate possible damage of the molecules under X-ray irradiation. Nonetheless, the total acquisition time was reduced as much as possible compatibly with an acceptable signal-to-noise ratio. The compounds in the form of finely ground powders were spread on a conducting adhesive tape attached to the sample holder. The BE scale was calibrated by setting the aliphatic component of the C 1s peak to 284.8 eV.[33] This allows us to correct the BE scale for the electrostatic charging due to the photoemission from the insulator samples. The spectra were smoothed, and the background due to the inelastically scattered electrons was subtracted by means of the Shirley method.[33] The curve-fitting analysis was carried out using the *XPSPEAK41* software.

5. Computational Details. All ab initio DFT calculations were carried out using the *Gaussian 03* package.[34] We used the standard double-ζ quality LanL2DZ basis set for all calculations. It applied the Dunning/Huzinaga full double-ζ (D95 V)[35] basis functions on the first row and the Los Alamos effective core potential plus DZ functions on all other atoms.[36] The LanL2DZ basis set incorporated the spin−orbit-averaged relativistic effects needed for the heavy atoms. Because of the lack of polarization functions in this basis set, the distance bond Pt−P may be overestimated.[37] To avoid this drawback, polarization d functions were added on the P atoms. For both the neutral and oxidized forms, we used the "hybrid" B3LYP functional.[38] For the $S = {}^1/_2$ cations, $\mathbf{1}^+$ unrestricted calculations were carried out. Calculations in CH_2Cl_2 were performed in the framework of the PCM[39] description, using CPCM.[40]

Acknowledgment. This work was supported by the Ministero dell'Istruzione, dell'Università e della Ricerca (MIUR), Programmi di Rilevante Interesse Nazionale (PRIN 2006−2007), and by the University of Pisa (Progetti di Ricerca 2006 Scienze e tecnologie dei nano/microsistemi).

Supporting Information Available: Curve-fitting analysis of the Pt 4f peaks measured for **1** (Figure S1), changes in the β frontier orbital energies for R = Bu^t, Me, and H in $\mathbf{1}^+$, in vacuo and in solution (Figure S2), linear fit between the energy shift of the NIR band and the difference of the dipole moment in solvent and in vacuo (Figure S3), complete ref 34, and X-ray crystallographic data of compound **1** in CIF format. This material is available free of charge via the Internet at http://pubs.acs.org.

(32) Krejčik, M.; Daněk, M.; Hartl, F. *J. Electroanal. Chem.* **1991**, *317*, 179.

(33) *Handbook of X-ray Photoelectron Spectroscopy*; Chastain, J., Ed.; Perkin-Elmer: Eden Praire, MN, 1992.

(34) Frisch, M. J.; Trucks, G. W.; Schlegel, H. B.; Scuseria, G. E.; Robb, M. A.; Cheeseman, J. R.; Montgomery, J. A., Jr.; Vreven, T.; Kudin, K. N.; Burant, J. C.; Millam, J. M.; Iyengar, S. S.; Tomasi, J.; Barone, V.; Mennucci, B.; Cossi, M.; Scalmani, G.; Rega, N.; Petersson, G. A.; Nakatsuji, H.; Hada, M.; Ehara, M.; Toyota, K.; Fukuda, R.; Hasegawa, J.; Ishida, M.; Nakajima, T.; Honda, Y.; Kitao, O.; Nakai, H.; Klene, M.; Li, X.; Knox, J. E.; Hratchian, H. P.; Cross, J. B.; Bakken, V.; Adamo, C.; Jaramillo, J.; Gomperts, R.; Stratmann, R. E.; Yazyev, O.; Austin, A. J.; Cammi, R.; Pomelli, C.; Ochterski, J. W.; Ayala, P. Y.; Morokuma, K.; Voth, G. A.; Salvador, P.; Dannenberg, J. J.; Zakrzewski, V. G.; Dapprich, S.; Daniels, A. D.; Strain, M. C.; Farkas, O.; Malick, D. K.; Rabuck, A. D.; Raghavachari, K.; Foresman, J. B.; Ortiz, J. V.; Cui, Q.; Baboul, A. G.; Clifford, S.; Cioslowski, J.; Stefanov, B. B.; Liu, G.; Liashenko, A.; Piskorz, P.; Komaromi, I.; Martin, R. L.; Fox, D. J.; Keith, T.; Al-Laham, M. A.; Peng, C. Y.; Nanayakkara, A.; Challacombe, M.; Gill, P. M. W.; Johnson, B.; Chen, W.; Wong, M. W.; Gonzalez, C.; Pople, J. A. *Gaussian 03*, revision C.02; Gaussian, Inc.: Wallingford, CT, 2004.

(35) (a) Stratmann, R. E.; Scuseria, G. E.; Frisch, M. J. *J. Chem. Phys.* **1998**, *109*, 8218. (b) Bauernschmitt, R.; Ahlrichs, R. *Chem. Phys. Lett.* **1996**, *256*, 454. (c) Casida, M. E.; Jamorski, C.; Casida, K. C.; Salahub, D. R. *J. Chem. Phys.* **1998**, *108*, 4439.

(36) (a) Hay, P. J. Wadt, W. R. *J. Chem. Phys.* **1985**, *82*, 270 and 299. (b) Wadt, W. R.; Hay, P. J. *J. Chem. Phys.* **1985**, *82*, 284.

(37) Fantucci, P.; Polezzo, S.; Sironi, M.; Bencini, A. *J. Chem. Soc., Dalton Trans.* **1995**, 4121.

(38) Becke, A. D. *J. Chem. Phys.* **1993**, *98*, 5648.

(39) Barone, V.; Cossi, M. *J. Phys. Chem. A* **1998**, *102*, 1995.

(40) Cossi, M.; Rega, N.; Scalmani, G.; Barone, V. *J. Comput. Chem.* **2003**, *24*, 669.